

# Ultrathin single-ion conducting polymer enabling a stable Li|Li<sub>1.3</sub>Al<sub>0.3</sub>Ti<sub>1.7</sub>(PO<sub>4</sub>)<sub>3</sub> interface

Zhen Chen<sup>a,b,c</sup>, Hai-Peng Liang<sup>a,b</sup>, Ziyuan Lyu<sup>a,b</sup>, Neelima Paul<sup>d</sup>, Giovanni Ceccio<sup>e</sup>,  
Ralph Gilles<sup>d</sup>, Maider Zarrabeitia<sup>a,b</sup>, Alessandro Innocenti<sup>a,b</sup>, Medina Jasarevic<sup>a,b</sup>,  
Guk-Tae Kim<sup>a,b</sup>, Stefano Passerini<sup>a,b,f,\*</sup>, Dominic Bresser<sup>a,b,\*</sup>

<sup>a</sup> Helmholtz Institute Ulm (HIU), 89081 Ulm, Germany

<sup>b</sup> Karlsruhe Institute of Technology (KIT), 76021 Karlsruhe, Germany

<sup>c</sup> Key Laboratory of Engineering Dielectric and Applications (Ministry of Education), School of Electrical and Electronic Engineering, Harbin University of Science and Technology, Harbin 150080, China

<sup>d</sup> Technical University of Munich (TUM), Heinz Maier-Leibnitz Zentrum (MLZ), 85748 Garching, Germany

<sup>e</sup> Nuclear Physics Institute of the Czech Academy of Sciences, 20568 Husinec-Rez, Czech Republic

<sup>f</sup> Sapienza University of Rome, Chemistry Department, Piazzale A. Moro 5, 00185 Rome, Italy

## ARTICLE INFO

### Keywords:

Solid-state electrolyte  
Polymer interlayer  
Single-ion conductor  
Lithium-metal battery  
Bipolar stacking

## ABSTRACT

NASICON-type Li<sub>1+x</sub>Al<sub>x</sub>Ti<sub>2-x</sub>(PO<sub>4</sub>)<sub>3</sub> (LATP) solid electrolytes have attracted great attention because of their high ionic conductivity, wide electrochemical stability window, pronounced chemical resistance, and low cost. However, the chemical instability of LATP against metallic lithium (Li<sup>0</sup>) poses a major challenge and hinders its application in solid-state lithium batteries. Herein, an ultrathin polysiloxane-based single-ion conductor (PSiO) serves as multifunctional protection interlayer to enhance the interfacial stability between LATP and Li<sup>0</sup>. PSiO effectively blocks the direct contact between Li<sup>0</sup> and LATP, regulates the homogeneous Li<sup>+</sup> flux at the Li|electrolyte interface, promotes the intimate contact between PSiO and Li<sup>0</sup> by forming Si – O – Li bonds, and generates an LiF-enriched Li|electrolyte interphase. As a result, it enables more than 2,000 h of stable cycling in symmetric PSiO@Li|PSiO@Li cells and superior rate capability and cycling stability in high-energy PSiO@Li|LiNi<sub>0.88</sub>Co<sub>0.09</sub>Mn<sub>0.03</sub>O<sub>2</sub> cells. The realization of well performing 2-layer bipolar stacked cells eventually demonstrates the great potential of this approach.

## 1. Introduction

Since their commercialization in the 1990s, lithium-ion batteries (LIBs) have greatly reshaped our daily life by fast proliferation in portable electronic devices, electric vehicles and energy storage grids [1–4]. Nevertheless, the capacity and energy density of LIBs are approaching the intrinsic limits of the utilized intercalation chemistry [2,5], and the globally growing demands call for new battery systems with even higher energy density and safety as well as longer lifespan [6]. Lithium metal (Li<sup>0</sup>), the so-called ‘holy grail’ anode material, possesses a very low electrochemical potential (-3.04 V vs. standard hydrogen electrode) and an unrivalled specific capacity (3860 mAh g<sup>-1</sup>) [7–9]. Accordingly, replacing graphite with Li<sup>0</sup> is anticipated to increase the gravimetric and the volumetric energy density of cells by 35% and 50%, respectively [10,11]. In fact, commercial lithium-metal batteries (LMBs)

had been launched already in the late 1980s by the Canadian company Moli Energy [12,13]. Nevertheless, these cells were called back owing to frequent accidents resulting from Li<sup>0</sup> dendritic deposition and high reactivity with the flammable liquid organic electrolyte. The increasingly intensive pursuit for advanced battery systems, however, has revitalized the interest in Li<sup>0</sup> as the anode and, hence, sparkingly extensive research on the stabilization of the Li|electrolyte interface [8,14].

One of the most prominent approaches to achieve this ambitious goal is the use of solid electrolytes (SEs), especially with regard to their commonly greater safety compared to liquid organic electrolyte systems. Of particular interest at present are so-called hybrid electrolyte systems, comprising, for instance, an inorganic solid phase and a polymer component. Such systems allow for beneficially combining the high ionic conductivity and thermal stability of the inorganic component, and

\* Corresponding authors at: Helmholtz Institute Ulm (HIU), 89081 Ulm, Germany.

E-mail addresses: [stefano.passerini@kit.edu](mailto:stefano.passerini@kit.edu) (S. Passerini), [dominic.bresser@kit.edu](mailto:dominic.bresser@kit.edu) (D. Bresser).

the high flexibility and intimate electrode|electrolyte contact of the polymer phase [15–17]. Nonetheless, when considering ‘simple’ mixtures of the two phases, a new fundamental challenge occurs, *i.e.*, the complex  $\text{Li}^+$  migration through the hybrid electrolyte and across the inorganic|polymer interfaces and interphases. Additionally, challenges of the single components such as the poor stability of high-performance inorganic electrolytes in contact with  $\text{Li}^0$  remain. In the case of the very well established NASICON-type  $\text{Li}_{1.3}\text{Al}_{0.3}\text{Ti}_{1.7}(\text{PO}_4)_3$  (LATP), for example, it is known that the  $\text{Ti}^{4+}$  cations are instantly reduced in contact with  $\text{Li}^0$ , resulting in the formation of a reactive and thus evolving interphase because of its mixed ionic/electronic conductivity (MCIs) [18]. Worst yet, such a reaction is both thermodynamically and kinetically favorable [9]. Taking these and other common challenges of SEs into account, it becomes clear that any potentially successful hybrid solution will have to be designed in a way that (i) there is no direct contact between the inorganic phase and the Li electrode, (ii) the  $\text{Li}^+$  ions can migrate through the inorganic phase and across the interfaces and interphases with the other electrolyte components, (iii) the electrolyte system remains easily processable and ensures intimate interfaces with the electrodes [19], and that (iv) a high degree of safety is maintained despite the incorporation of additional organic components, while simultaneously (v) showing a homogeneous and non-dendritic lithium deposition and (vi) providing a sufficient electrochemical stability towards oxidation to allow for the use of high-energy cathode materials such as Ni-rich  $\text{LiNi}_{1-x-y}\text{Co}_x\text{Mn}_y\text{O}_2$  (NCM).

In a previous study [20], we constructed a hybrid electrolyte comprising LATP, electrochemically inactive poly(vinylidene fluoride-trifluoroethylene) (PVdF-TrFE), and an ionic liquid-based electrolyte, comprising 0.3LiFSI (lithium bis(fluorosulfonyl)imide) in 0.35Py<sub>14</sub>FSI (*N*-butyl-*N*-methyl-pyrrolidinium bis(fluorosulfonyl)imide) and 0.35Py<sub>14</sub>TFSI (*N*-butyl-*N*-methyl-pyrrolidinium bis(trifluoromethanesulfonyl)imide), hereinafter abbreviated as MILE. In this hybrid electrolyte system, LATP and MILE provide the ionic conductivity, while PVdF-TrFE connects the ceramic particles to form a 3D network and to enable the preparation of free-standing and flexible electrolyte films. MILE additionally promotes a better wettability of the electrodes and reduces the interfacial resistances. While this system showed high ionic conductivity, facile processability owing to the flexible nature of the resulting electrolyte sheets, and very good compatibility with Ni-rich NCM, the interfacial stability with  $\text{Li}^0$  remained an issue, resulting in increasing interfacial resistances and dendritic lithium growth [18]. In another recent study, we reported a new single-ion conducting polymer electrolyte (SIPE) based on a polysiloxane backbone (PSiO) [21]. The chemical design of the free-standing polymer electrolyte membranes composed of PSiO blended with poly(vinylidene fluoride-*co*-hexafluoropropylene) (PVdF-HFP) enabled the realization of a suitable interface and interphase with the  $\text{Li}^0$  electrode, homogeneous  $\text{Li}^+$  flux, and smooth, dendrite-free lithium deposition.

Inspired by these findings, we developed  $\text{Li}^0$  electrodes coated with an ultrathin layer of the single-ion conducting PSiO (PSiO@Li) to simultaneously prevent the physical contact between the LATP-based hybrid electrolyte and  $\text{Li}^0$ , and ensure the homogeneous  $\text{Li}^+$  flux across the electrode|electrolyte interface. These PSiO@Li electrodes were realized *via* dip-coating, which is an easily scalable method, and the PSiO interlayer enables a dramatically improved cycle life of the resulting LMB cells.

## 2. Results and discussion

### 2.1. Physicochemical characterization of the PSiO coating

In the first step, the surface morphology of pristine Li and PSiO@Li was investigated *via* scanning electron microscopy (SEM). Generally, the pristine Li (Figs. 1a and S1a) shows a very smooth surface. The apparent line traces are predominantly attributed to the extrusion step during fabrication and a higher magnification (inset in Fig. 1a) reveals some

white dots, which are assigned to  $\text{Li}_2\text{CO}_3$  formed during the fabrication process under a mixture of argon and  $\text{CO}_2$  [22]. After coating PSiO on the lithium surface, the insulating nature of PSiO reduces the overall clarity of the SEM micrograph (Figs. 1b and S1b). Notably, the line traces are still visible, implying that the PSiO layer is rather thin. The homogeneity of the PSiO coating of the PSiO@Li electrode was corroborated by conducting energy dispersive X-ray spectroscopy (EDS), revealing the homogeneous distribution of N, C, O, S, F, and Si (Fig. S2). Fig. 1c shows the Fourier transform infrared (FT-IR) spectroscopy data obtained for PSiO@Li in comparison with the data recorded for pure PSiO powder. The main bands found for PSiO@Li (in orange), *i.e.*, C–H ( $1454\text{ cm}^{-1}$ ), Si–C ( $1266\text{ cm}^{-1}$ ), C–F ( $1196\text{ cm}^{-1}$ ), and S=O ( $1329\text{ cm}^{-1}$ ,  $1125\text{ cm}^{-1}$ ), are well in line with those of the PSiO reference (in blue) [21], confirming the successful coating of the  $\text{Li}^0$  foil with PSiO. The stretching vibration of the C=O bond shifts from  $1715\text{ cm}^{-1}$  to  $1731\text{ cm}^{-1}$ , which is probably due to the interaction with  $\text{Li}^0$  [23]. Similarly, a red shift of the band associated to the Si–O bond from  $1057\text{ cm}^{-1}$  to  $1070\text{ cm}^{-1}$  occurred concomitantly with a reduced intensity. This observation indicates the formation of Si–O–Li bonds, ensuring a highly intimate contact between the PSiO coating and the  $\text{Li}^0$  surface [24,25]. Besides, the sharp peak located at  $881\text{ cm}^{-1}$  and the broad peak occurring between  $1358\text{ cm}^{-1}$  and  $1610\text{ cm}^{-1}$  are attributed to the native surface contaminants on the  $\text{Li}^0$  foil, particularly,  $\text{Li}_2\text{CO}_3$  [26], and the peak at  $1675\text{ cm}^{-1}$  corresponds to the stretching vibration of the C=O bond from residual NMP traces (see Fig. S3) [27].

Subsequently, we performed neutron depth profiling (NDP) to nondestructively determine the thickness of the PSiO coating on the  $\text{Li}^0$  foil from the lithium concentration profile [28–31]. Both triton particles (Fig. S4) as well as  $\alpha$  particles (Fig. 1d, e) were analyzed to determine the Li distribution profiles, as both carry similar information. In the present case, though, we relied more on the  $\alpha$  particle profiles, since they offered a comparatively higher energy resolution than the triton particles in the region close to the sample surface. The plots of the Li concentration vs. mass loading of pristine Li ( $50\text{ }\mu\text{m}$  and  $300\text{ }\mu\text{m}$ ) and PSiO@Li ( $50\text{ }\mu\text{m}$  and  $300\text{ }\mu\text{m}$ ) are displayed in Fig. 1d and e, respectively. The term mass loading is defined as the product of sample density times the depth of reaction origin where the neutron reacts with the  $^6\text{Li}$  isotope [32]. The thickness of PSiO was estimated by the ratio of the mass loading difference between pristine Li and PSiO@Li and the true density of PSiO ( $1.48\text{ g cm}^{-3}$ ). The thickness of the PSiO polymer film was calculated to be  $80 \pm 14\text{ nm}$  and  $140 \pm 14\text{ nm}$  for PSiO@Li ( $50\text{ }\mu\text{m}$  and  $300\text{ }\mu\text{m}$ ) (Table S1), respectively. Considering that the theoretical resolution is around  $30\text{ nm}$  for a standard NDP geometry, due to statistical processes and intrinsic resolution of the instrument, we can roughly estimate the average thickness of the PSiO coating to be  $110 \pm 30\text{ nm}$ . It is worth mentioning that such an ultrathin interlayer barely has any impact on the gravimetric and volumetric energy densities.

### 2.2. Impact of the PSiO interlayer on the cell performance

To investigate the impact of the PSiO interlayer on the interfacial stability between  $\text{Li}^0$  and the hybrid LATP/PVdF-TrFE/MILE electrolyte, symmetric PSiO@Li||PSiO@Li cells were assembled for lithium stripping-plating tests (at  $0.1\text{ mA cm}^{-2}$ ) and compared to symmetric Li||Li cells without the PSiO coating (Fig. 2a). In the case of the Li||Li cells, after an initial decrease, the overpotential steadily increases, before eventually stabilizing at ca.  $66\text{ mV}$  after around  $130\text{ h}$ . After about  $390\text{ h}$ , though, a rapid decline of the overpotential was observed, indicating the occurrence of a ‘soft short-circuit’ [20]. The PSiO@Li||PSiO@Li cell exhibited an initial overpotential of  $260\text{ mV}$  (Fig. 2a), *i.e.*, about 3 times higher than that of the Li||Li cell ( $89\text{ mV}$ ), which can be reasonably explained by the introduction of the PSiO coating, resulting in higher interfacial resistance. Subsequently, the overpotential sharply decreased owing to the improved interfacial contact and Li surface reorganization, including the breakdown of the native passivation layer and the formation of a less resistive solid electrolyte interphase (SEI) [33–35]. After

cycling for about 250 h, the overpotential stabilized at  $\sim 80$  mV and remained essentially stable with a very minor increase by about 10 mV after 2,000 h, when the cell was stopped for the *ex situ* analysis. This outstanding cycling stability supports for the formation of highly stable interface/interphase between the  $\text{Li}^0$  electrode and the hybrid electrolyte, benefitting from the essentially single-ion conductivity (Fig. S5) and high stability towards reduction (Fig. S6) of the electrolyte system in PSiO@Li comprising cells. In fact, the subsequent *ex situ* FT-IR analysis (Fig. S7) revealed that the protective PSiO coating was still present on the  $\text{Li}^0$  surface despite its very small thickness ( $110 \pm 30$  nm).

In a next step, the electrochemical performance of full-cells composed of  $\text{LiNi}_{0.88}\text{Co}_{0.09}\text{Mn}_{0.03}\text{O}_2$  (NCM<sub>88</sub>) at the positive electrode, PSiO@Li (or pristine Li) at the negative electrode and the hybrid LATP/PVdF-TrFE/MILE electrolyte was investigated. Fig. 2b–e compares the rate capability and cycling stability of the PSiO@Li||NCM<sub>88</sub> and Li||NCM<sub>88</sub> cells. Initially, at a dis-/charge rate of 0.05C (1C =  $200 \text{ mA g}^{-1}$ ), the discharge capacity ( $213 \text{ mAh g}^{-1}$ ) and initial Coulombic efficiency (ICE, 91.9%) of the PSiO@Li||NCM<sub>88</sub> cell (Fig. 2b, d) were slightly lower compared to the Li||NCM<sub>88</sub> cell ( $217 \text{ mAh g}^{-1}$  and 92.6%; Fig. 2c, d). Moreover, the Li||NCM<sub>88</sub> cell provided slightly higher capacities at 0.1C ( $210 \text{ mAh g}^{-1}$  vs.  $208 \text{ mAh g}^{-1}$ ) and 0.2C ( $199 \text{ mAh g}^{-1}$  vs.  $198 \text{ mAh g}^{-1}$ ). This minor difference in capacity has been somehow expected given the presence of the additional PSiO interlayer. When further increasing the dis-/charge rate, however, the PSiO@Li||NCM<sub>88</sub> cell outperformed the Li||NCM<sub>88</sub> cell. Notably, above 0.5C, the superior

performance of PSiO@Li as the negative electrode becomes highly evident: the PSiO@Li||NCM<sub>88</sub> cell retained reversible specific capacities of  $153 \text{ mAh g}^{-1}$  at 0.75C and  $125 \text{ mAh g}^{-1}$  at 1C, which is about 37% and 140% higher than the capacities provided by the Li||NCM<sub>88</sub> cell (i.e.,  $112 \text{ mAh g}^{-1}$  at 0.75C and  $52 \text{ mAh g}^{-1}$  at 1C). These findings indicate that the implementation of the PSiO interlayer is critical for enhancing the dis-/charge performance at high current densities, presumably owing to its single-ion conducting nature and a reduced detrimental impact of reversed cell polarization at elevated currents. When subsequently decreasing the dis-/charge rate back to 0.2C, the PSiO@Li||NCM<sub>88</sub> cell was capable of retaining a reversible capacity of  $198 \text{ mAh g}^{-1}$ , corresponding to a capacity retention of 99.7%. The Li||NCM<sub>88</sub> cell delivered a somewhat lower specific capacity of  $196 \text{ mAh g}^{-1}$  and achieved a capacity retention of only 98.5%.

The long-term cycling stability of PSiO@Li||NCM<sub>88</sub> and Li||NCM<sub>88</sub> cells is displayed in Fig. 2e. After the initial formation cycles, both cells were subjected to 500 cycles at 1C. The PSiO@Li||NCM<sub>88</sub> cell retained a higher capacity of  $128 \text{ mAh g}^{-1}$  (vs.  $118 \text{ mAh g}^{-1}$ ), being very well in line with the results of the rate capability test. Even more importantly, the Li||NCM<sub>88</sub> cell showed a fast capacity decay, quickly reaching the ‘End-of-Life’ (EoL) threshold of 80% capacity retention after only 74 cycles. Differently, the PSiO@Li||NCM<sub>88</sub> cell hit the EoL threshold after 304 cycles, which is a dramatic improvement by a factor of 4. After 500 cycles, the PSiO@Li||NCM<sub>88</sub> and Li||NCM<sub>88</sub> cells retained a specific capacity of 81 and  $42 \text{ mAh g}^{-1}$ , respectively, corresponding to a capacity

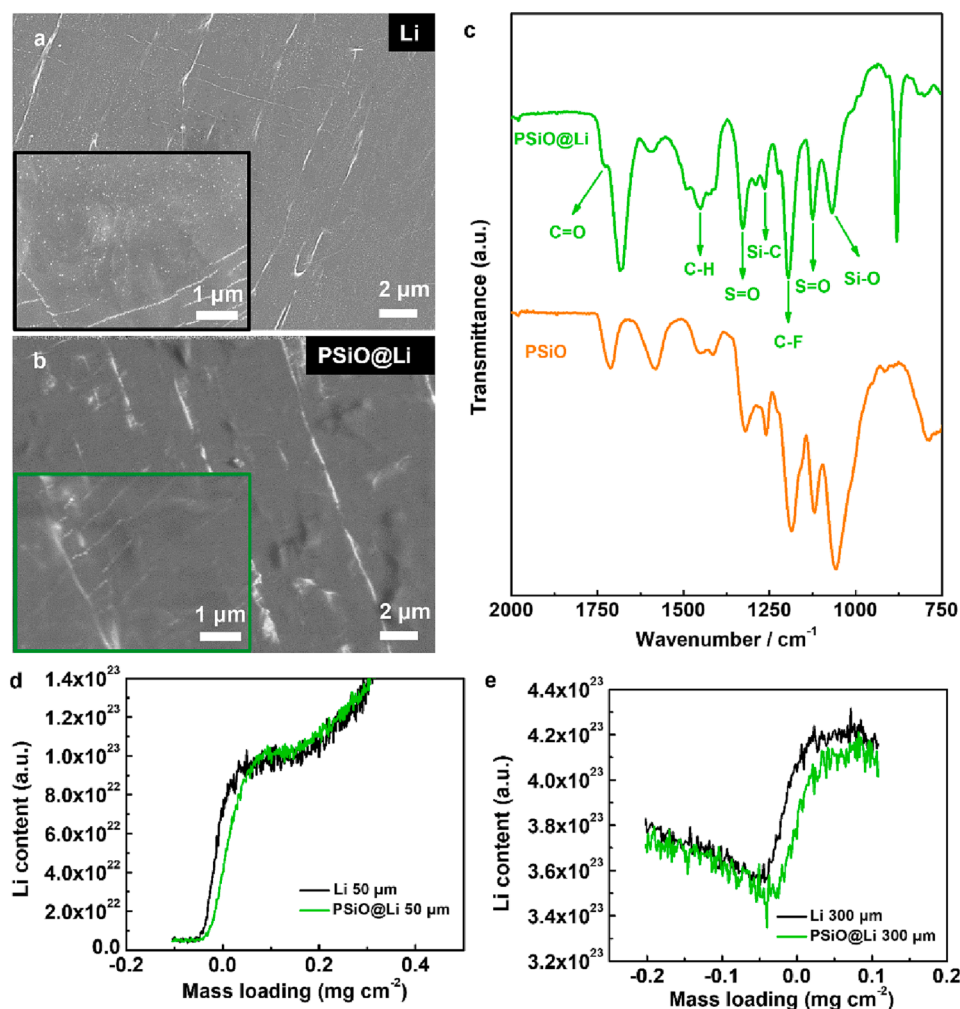
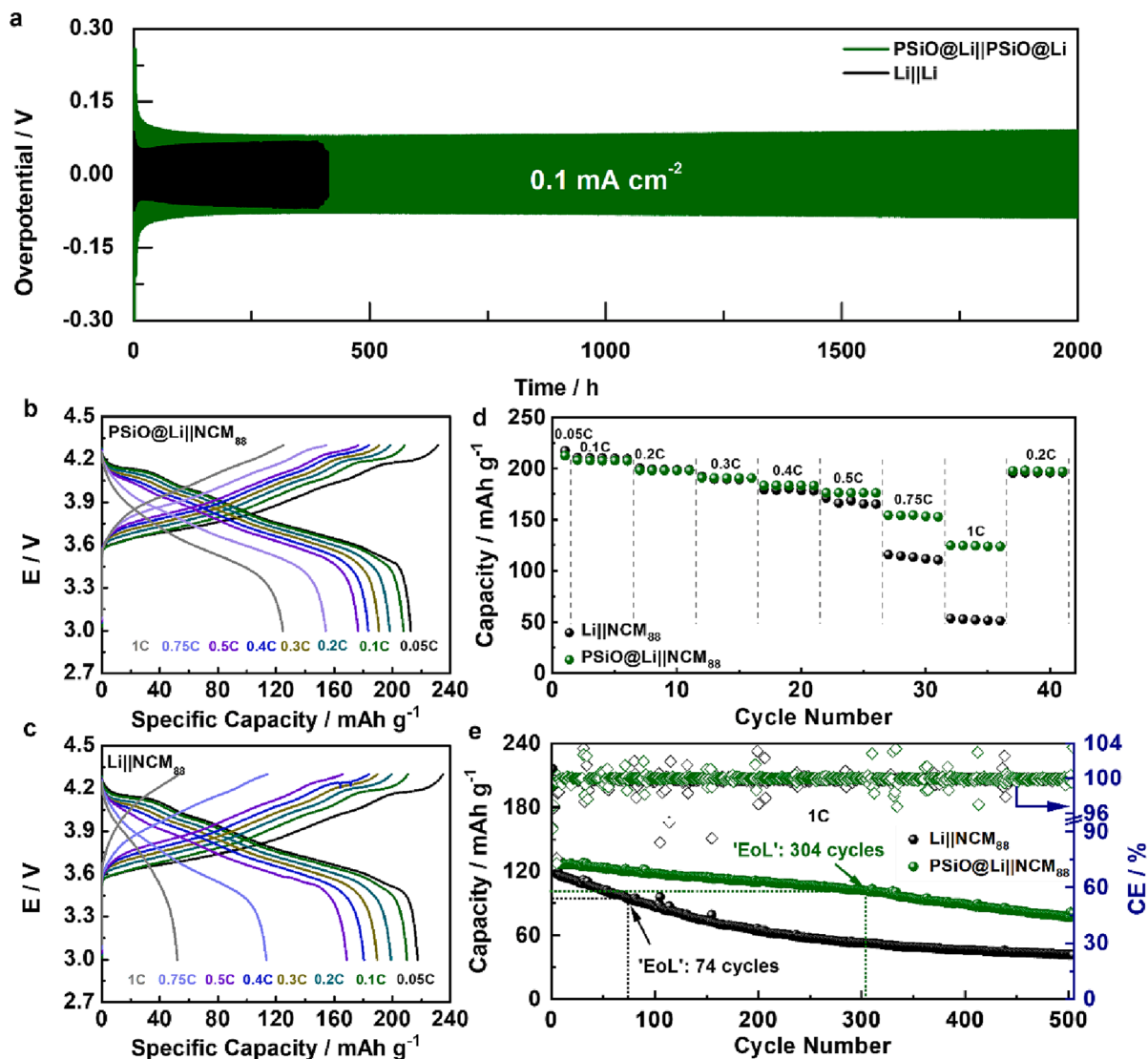


Fig. 1. The surface morphology of (a) pristine Li and (b) PSiO-coated Li (PSiO@Li). (c) FT-IR spectra of PSiO@Li (in green) and PSiO powder (in orange). (d, e) Li density profiles of PSiO@Li (in green) and pristine Li (in black) as a function of mass loading (using the  $\alpha$  particle energy loss profile) to determine the thickness of the PSiO coating on (d) 50  $\mu\text{m}$  and (e) 300  $\mu\text{m}$  thick  $\text{Li}^0$  foil.



**Fig. 2.** (a) Comparison of the lithium stripping-plating experiment conducted with Li||Li cells (in black) and PSiO@Li||PSiO@Li cells (in green), both comprising the hybrid LATP/PVdF-TrFE/MILE electrolyte. (b-d) Evaluation of the rate capability of the (b, d) PSiO@Li||NCM<sub>88</sub> and (c, d) Li||NCM<sub>88</sub> cells along with the corresponding dis-/charge profiles. (e) Long-term cycling performance of the PSiO@Li||NCM<sub>88</sub> and Li||NCM<sub>88</sub> cells at 1C. The temperature was set to 20 °C for all experiments.

retention of 62.8% and 35.4%. This substantially enhanced performance of the PSiO@Li||NCM<sub>88</sub> cell originates not least from the higher average CE of 99.91% compared to only 99.77% for the Li||NCM<sub>88</sub> cell. These results further confirm the effectiveness of the PSiO interlayer for stabilizing the interface between the Li<sup>0</sup> electrode and the hybrid electrolyte and, thus, improving the rate capability as well as the long-term cycling stability.

### 2.3. Ex situ investigation on the enhanced performance enabled by PSiO coating

Following the 500 cycles at 1C (Fig. 2e), the negative and positive electrodes were recovered and analyzed *via* SEM in a first step. Figs. 3 and S8 show the surface morphology of the cycled PSiO@Li (denoted as C<sub>PSiO@Li</sub>) and Li (marked as C<sub>Li</sub>) electrodes, respectively. The surface of C<sub>PSiO@Li</sub> (see Fig. S8a, b for lower magnifications and Fig. 3a for an image at higher magnification) was relatively clean and flat, *i.e.*, free of dendritic Li. On the contrary, C<sub>Li</sub> exhibited a rougher surface (Fig. S8c, d) and plenty of ‘corrosion pits’ (highlighted with dashed red lines). Taking a closer look at these pits (Fig. 3b), revealed agglomerated

particles, penetrating into the bulk lithium electrode. Additionally, some fibrous Li dendrites (indicated by the red arrow in Fig. 3b) were observed beneath these particles. The *ex situ* EDS analysis of such ‘particle island’ features on C<sub>Li</sub> (Fig. S9) showed that these particles are composed of aluminum, titanium, phosphorus, and oxygen, confirming that they are composed of LATP. The resulting parasitic reactions, including the reduction of Ti<sup>4+</sup> and inhomogeneous Li deposition, are causing the inferior cycling stability and CE of the Li||NCM<sub>88</sub> cells. The PSiO interlayer apparently prevents such penetration of the LATP particles into the lithium electrode, as schematically depicted in Fig. 3c, d, eventually leading to the substantially ameliorated long-term cycling stability of PSiO@Li||NCM<sub>88</sub> cells. In fact, the *ex situ* SEM analysis of the cycled NCM<sub>88</sub> cathode did not show any appreciable difference (Fig. S10).

In a second step, the cycled electrodes were studied *via* *ex situ* X-ray photoelectron spectroscopy (XPS). Again, the analysis of the cycled NCM<sub>88</sub> positive electrode (Fig. S11) did not reveal any significant difference for the two cells, underlining that the reactions occurring at the negative electrode are decisive. The *ex situ* XPS data obtained for C<sub>PSiO@Li</sub> and C<sub>Li</sub> before and after 20 min of Ar<sup>+</sup> sputtering are

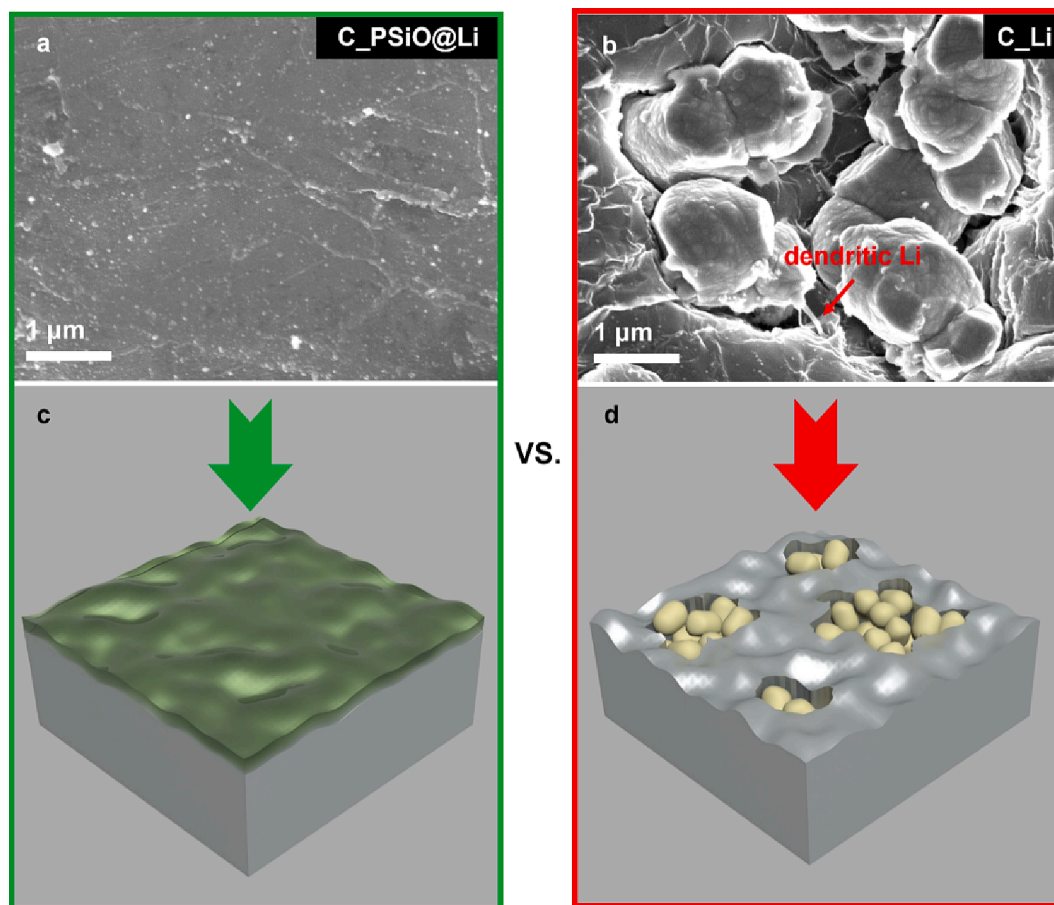


**Fig. 3.** *Ex situ* SEM analysis of (a) cycled PSiO@Li (C\_PSiO@Li) and (b) cycled Li (C\_Li) electrodes recovered from the PSiO@Li||NCM<sub>88</sub> and Li||NCM<sub>88</sub> cells after 500 cycles at 1C (Fig. 2e). (c, d) Schematic illustration depicting the protective effect of the PSiO coating on the Li<sup>0</sup> electrode.

presented in Fig. 4. The chemical composition of the SEI formed on the two negative electrodes showed significant differences at the outmost surface, while less differences were observed after sputtering, *i.e.*, for the inner layers of the SEI. In the case of C\_PSiO@Li, PSiO related features are clearly detectable, *i.e.* -Si-C- (at 282.5 eV - C 1s), RC-(C=O)-O (at 289.6 eV - C 1s and 531.4 eV - O 1s), -Si-O-Si- (at 532.0 eV - O 1s), and -S-C- (at 163.5 eV - S 2p) [36–38]. The presence of -Si-C- and -Si-O-Si bonds is also apparent from the Si 2p spectra presented in Fig. S12 [37,39]. However, the signals associated to FSI and TFSI and their decomposition products are also observed, *i.e.*, at 688.6 eV (F 1s), 400.0 eV (N 1s) and 169.5 eV (S 2p) [40,41], which are rather weak compared to those observed for C\_Li, indicating a rather thin SEI and corroborating that the PSiO interlayer mitigates the MILE decomposition. This is further supported by the substantially higher intensity of the O = C-O-C features in the C 1s and O 1s spectra of C\_Li, as these species are presumably resulting from the electrode rinsing step with DMC after disassembling the cells, highlighting the generally reduced reactivity of the PSiO-coated Li. The C\_PSiO@Li electrode showed almost no reactivity with DMC, confirming that the PSiO interlayer was well preserved also after 500 cycles.

The thickness of the SEI can be roughly estimated using Tanuma's equation, which considers the inelastic mean free path (IMPF) of a selected element and the photon energy [42]. Owing to the presence of the PSiO coating in the case of the PSiO@Li electrode, we used the Li photoelectrons for the cycled Li electrode and the Si photoelectrons for PSiO@Li. Since we did not detect any Li metal signal for the cycled Li electrodes, the SEI is presumably thicker than 10 nm. In the case of the cycled PSiO@Li electrodes, the SEI was thinner, since we detected Si photoelectrons from the PSiO, indicating that the SEI was less than 10

nm in this case, approximately 8–9 nm.

After sputtering, *i.e.*, closer to the Li electrode surface, the SEI of C\_Li and C\_PSiO@Li was rather similar with the first main difference being the more pronounced presence of FSI and TFSI decomposition products in the case of C\_Li, specifically, Li<sub>3</sub>N (N 1s) and Li<sub>2</sub>S (S 2p) [40,43]. The second difference is the higher fraction of LiF found for C\_PSiO@Li SEI, which accounted to 3.1 at% vs. 1.6 at% in the case of C\_Li. This indicates that the presence of the PSiO interlayer promotes the formation of a LiF-enriched SEI close to the Li<sup>0</sup> side, which is commonly expected to yield a more stable interphase [14]. In addition with the other Li-bearing phases such as Li<sub>x</sub>SiO<sub>y</sub>, which have also been reported as very beneficial [25], the SEI formed in presence of PSiO appears to enable a more homogeneous Li<sup>+</sup> flux and deposition, allowing for the superior rate capability and capacity retention observed for PSiO@Li.

#### 2.4. Proof of concept in 2-layer bipolar stacked cells

To demonstrate the feasibility of realizing bipolar stacked cells with this cell chemistry, 2-layer [(-)SUS|PSiO@thin Li|hybrid electrolyte|NCM<sub>88</sub>|Al|SUS|PSiO@thin Li|hybrid electrolyte|NCM<sub>88</sub>|Al|SUS(+)] cells (denoted as B2\_PSiO@thin Li||NCM<sub>88</sub>) were assembled as a proof of concept. The configuration of this cell is depicted schematically in Fig. 5a. Stainless steel (SUS) was used as the bipolar plate (BP) to connect the two cells. It shall be mentioned that the Li<sup>0</sup> anode was only 20 μm thick in this setup. At 0.05C the B2\_PSiO@thin Li||NCM<sub>88</sub> cells delivered an initial specific discharge capacity of 204 mAh g<sup>-1</sup> and an ICE of 86.8% when cycled between 8.6 and 6.0 V (Fig. 5b, c). Increasing the dis-/charge rate to 0.1C resulted in a minor decrease in capacity with about 197 mAh g<sup>-1</sup>. Upon cycling, a mild decline in capacity was

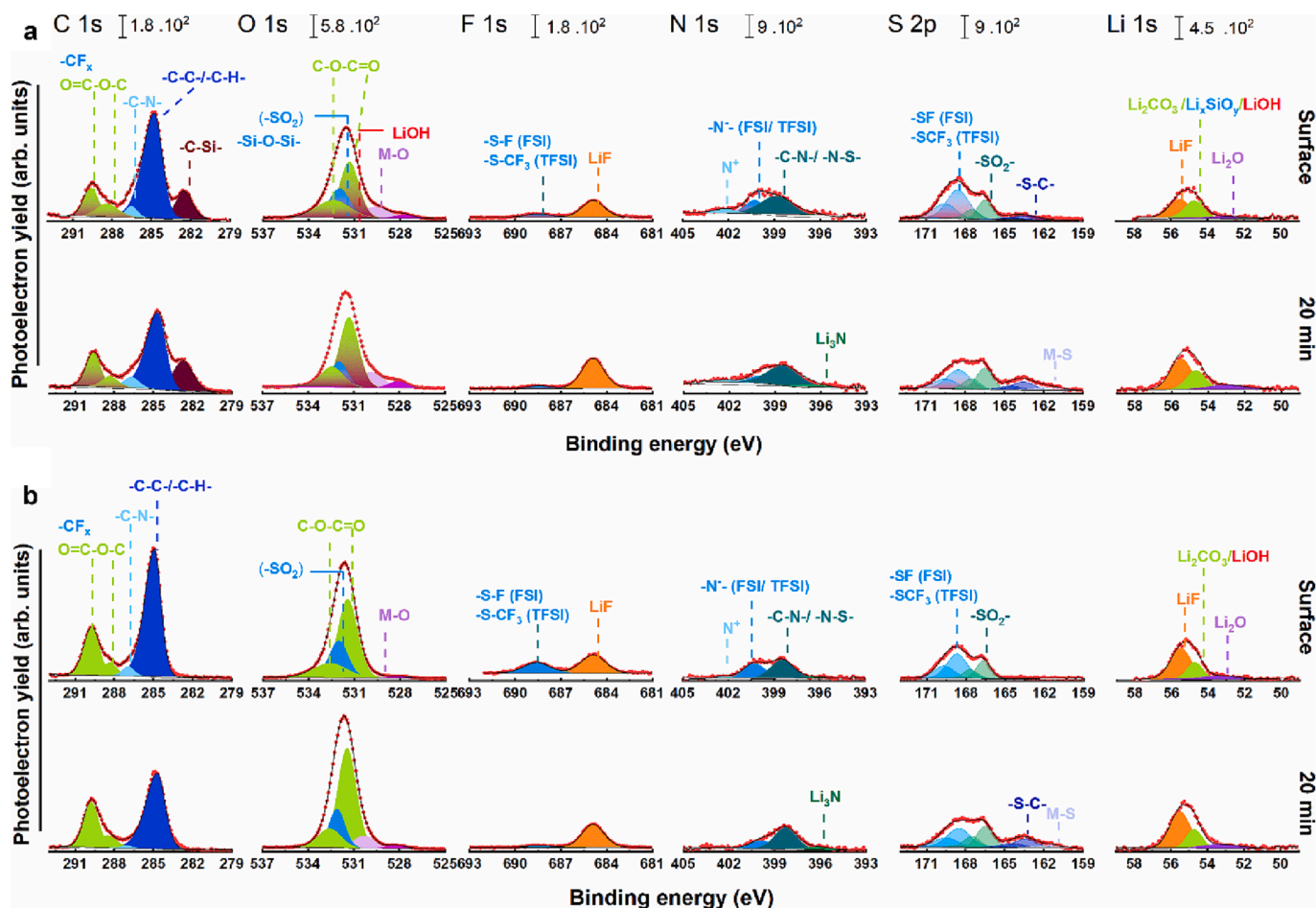


Fig. 4. Comparison of the C 1s, O 1s, F 1s, N 1s, S 2p, and Li 1s detail spectra before and after 20 min of  $\text{Ar}^+$  sputtering of (a) C\_PSiO@Li and (b) C\_Li electrodes recovered from the PSiO@Li||NCM<sub>88</sub> and Li||NCM<sub>88</sub> cells after 500 cycles at 1C.

observed, resulting in a capacity retention of 86.4% after 30 cycles. This minor decline in capacity presumably originates from the cell setup, which generally magnifies the fading of each single unit cell, as also evidenced by the lower average CE of 97.8% and the greater increase of the IR drop upon cycling (Fig. 5d). This is also reflected by a slight increase of the bulk resistance from 30  $\Omega$  to 41  $\Omega$  after 20 cycles (Fig. S13). Differently, the interfacial resistance decreases slightly from about 450  $\Omega$  to 340  $\Omega$ , which we assign to an improving interfacial contact at the electrode|electrolyte interfaces upon cycling. This antidromic behaviour in combination with the lower CE indicates that the decrease in capacity is mainly related to a decreasing utilization of the cathode active material – presumably due to the non-perfectly aligned electrodes in this bipolar setup. Nevertheless, the 2-layer bipolar cell still exhibited an impressive performance compared to previous studies [44–47]. Furthermore, the cycled and eventually charged bipolar cell was capable of powering a series of green LED lights (Fig. 5e, Video S1) for more than 2 min without an obvious decrease in light intensity.

### 3. Conclusion

In this work, we developed a highly efficient strategy to enhance the interfacial stability between LATP and  $\text{Li}^0$  by dip-coating the Li foil with an ultrathin polysiloxane-based single-ion conducting polymer layer (PSiO). The intimate contact between this PSiO coating and  $\text{Li}^0$  was evidenced by the formation of Si–O–Li bonds. The PSiO layer serves as a multi-functional protection interlayer, (i) preventing the direct contact between LATP and  $\text{Li}^0$  to avoid the reduction of LATP and the penetration of LATP into the  $\text{Li}^0$  foil, (ii) forming a LiF-rich inner SEI

region to further stabilize the interface, and (iii) regulating the  $\text{Li}^+$  flux at the electrode|electrolyte interface to ensure homogeneous lithium stripping/plating. As a result, symmetric PSiO@Li||PSiO@Li cells exhibited an excellent cycle life, exceeding 2,000 h of lithium stripping and plating. The PSiO@Li||NCM<sub>88</sub> cells revealed a substantially enhanced rate capability and capacity retention with 304 cycles at 1C until the capacity decreased below 80% of the initial value, compared to only 74 cycles without the PSiO interlayer. Maybe even more remarkably, the average Coulombic efficiency was as high as 99.91%, benefitting from the LiF and  $\text{Li}_x\text{SiO}_y$  enriched interphase close to the  $\text{Li}^0$  electrode and the absence of any pitting corrosion, which came along with the penetration of LATP particles into the lithium electrode in the case of the Li||NCM<sub>88</sub> cells. These benefits render the ultrathin PSiO interlayer a very promising approach to stabilize the Li|LATP interface and, thus, enable their commercial exploitation. To underline this, a proof of concept 2-layer bipolar stacked cell was realized, showing very good cycling stability and performance.

### 4. Experimental section

The preparation and handling of the PSiO@Li electrodes, LATP/PVdF-TrFE dry films, LATP/PVdF-TrFE/MILE electrolytes, Li||Li cells, PSiO@Li||PSiO@Li cells, Li||NCM<sub>88</sub> cells, PSiO@NCM<sub>88</sub> cells, bipolar stacked cells, and all *ex situ* samples were always performed in the dry room with a dew point of less than  $-60^\circ\text{C}$  at an ambient temperature of  $20^\circ\text{C}$ .

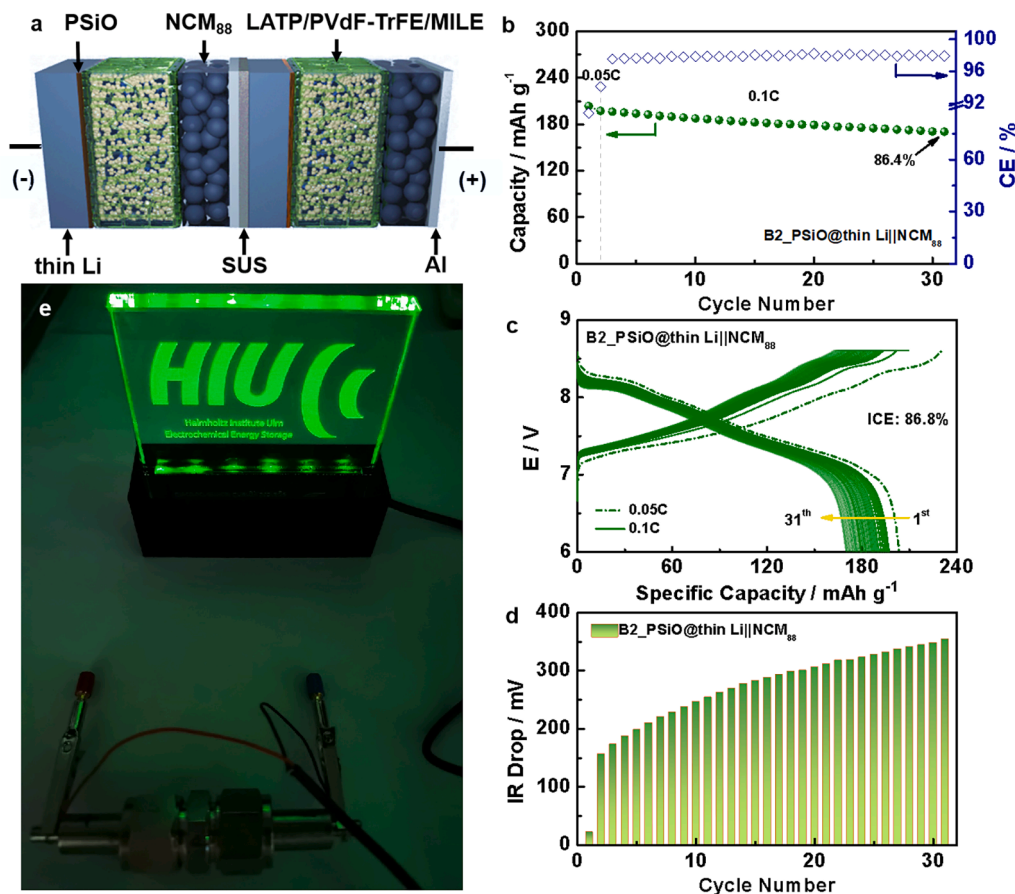


Fig. 5. (a) Schematic illustration of the B2\_PSiO@thin Li||NCM<sub>88</sub> bipolar stacked cell configuration; (b) cycling performance at 0.1C with a plot of the specific capacity vs. the cycle number; (c) the corresponding dis-/charge profiles of the complete stack; (d) the evolution of the IR drop upon cycling; (e) photograph of the B2\_PSiO@thin Li||NCM<sub>88</sub> cell powering a series of green LED lights.

#### 4.1. Hybrid electrolyte preparation

The synthesis of  $\text{Li}_{1.3}\text{Al}_{0.3}\text{Ti}_{1.7}(\text{PO}_4)_3$  (LAMP) and the preparation of the LAMP/PVdF-TrFE/MILE hybrid film was conducted as reported earlier [9,20,35]. In brief, dry LAMP/PVdF-TrFE membranes were prepared using a phase inversion method with a mass ratio of 92:8. The membranes were cut to a size of 1.5 cm × 2 cm. Then, 100  $\mu\text{L}$  of MILE, i. e., 0.3LiFSI-0.35Py<sub>14</sub>FSI-0.35Py<sub>14</sub>TFSI were added into the LAMP/PVdF-TrFE film. Afterwards, an ambient vacuum was applied to facilitate the infiltration of MILE into the pores of LAMP/PVdF-TrFE film. Excess MILE was squeezed out to avoid any free-flowing liquid electrolyte. The maximum porosity of the LAMP/PVdF-TrFE film, filled with the MILE, was about 33%, suggesting a weight ratio of about 24%.

#### 4.2. Preparation of PSiO-coated Li (PSiO@Li)

PSiO was synthesized according to a procedure described by Liang et al. [21]. To prepare the PSiO@Li sample, the as-obtained PSiO powder was dissolved in *N*-methyl-2-pyrrolidone (NMP; Aldrich) with a concentration of 0.5 wt%. A piece of Li<sup>0</sup> with a thickness of 500  $\mu\text{m}$  (Honjo; herein simply referred to as 'Li') or a piece of Li<sup>0</sup> with a thickness of 20  $\mu\text{m}$  deposited on Cu foil (Honjo; herein referred to as 'thin Li') was immersed in the PSiO in NMP solution for 4 min. Subsequently, the residual NMP was immediately removed under vacuum to obtain the PSiO-coated Li (PSiO@Li).

#### 4.3. Electrode fabrication and cell assembly

To prepare the  $\text{LiNi}_{0.88}\text{Co}_{0.09}\text{Mn}_{0.03}\text{O}_2$  (NCM<sub>88</sub>) positive electrodes,

firstly, 92 wt% of NCM<sub>88</sub> (POSCO), 4 wt% of C-ENERGY Super C65 (Imerys) and 4 wt% of polyvinylidene difluoride (PVdF; Solvay 6020) were mixed with an appropriate amount of NMP using a slurry mixer. The doctor-blade technique was adopted to cast the above-obtained slurries on battery-grade Al foil. The as-obtained wet electrode sheets were pre-dried in an oven at 60 °C. Afterwards, electrode disks ( $\Phi$ : 12 mm) were punched out of these pre-dried sheets and then transferred into a Büchi for vacuum drying (pressure: 10<sup>-3</sup> mbar; temperature: 100 °C; time: 12 h). All the electrodes were pressed at 10 t for 10 s to flatten the electrode surface, reduce the electrode porosity and improve the contact between the electrode and the current collector. The average NCM<sub>88</sub> mass loading was  $2.5 \pm 0.1 \text{ mg cm}^{-2}$ .

Symmetric Li||Li and PSiO@Li||PSiO@Li cells were assembled in two-electrode pouch cells using Ni as the current collector. The current density for Li stripping-plating tests was fixed at 0.1 mA cm<sup>-2</sup> and the specific areal capacity of each cycle was fixed at 0.2 mAh cm<sup>-2</sup>. The Li||NCM<sub>88</sub> and PSiO@Li||NCM<sub>88</sub> mono-layer cells were also assembled in two-electrode pouch cells using Ni and Al as the current collector for the counter electrode and the working electrode, respectively. The voltage range was set to 3.0–4.3 V. The bipolar stacked cells were assembled in two-electrode Swagelok-type cells. The voltage range was set to 6.0–8.6 V.

For both kinds of cells, a dis-/charge rate of 1C corresponds to a specific current of 200 mA g<sup>-1</sup>. The testing temperature was always fixed at 20 °C in a climatic chamber (Binder). For the evaluation of the rate capability, the cells were initially cycled at 0.05C for one formation cycle, and then subjected to five cycles at various C rates spanning from 0.1C to 1C before getting back to 0.2C. For the cycling performance test, the cells were cycled at 0.05C for one cycle and at 0.1C for three cycles

before subjecting them to 500 cycles at 1C. The bipolar stacked 2-layer cells were cycled for one cycle at 0.05C and 30 cycles at 0.1C.

#### 4.4. Physicochemical and electrochemical characterisation

The morphology of all samples was examined by scanning electron microscopy (SEM; ZEISS EVO MA 10). The true density of PSiO was determined using an Ultrapyc 1200e Automatic Gas Pycnometer. Neutron depth profiling (NDP) was performed on the PSiO@Li samples to measure the thickness of the PSiO coating. NDP is a neutron absorption analytical technique having a high detection sensitivity for  ${}^6\text{Li}$  isotope from the  ${}^6\text{Li}(n,\alpha){}^3\text{H}$  nuclear reaction. The interaction of each neutron with a  ${}^6\text{Li}$  isotope creates a triton ( ${}^3\text{H}$ ) and an alpha  $\alpha$  ( ${}^4\text{He}$ ) particle with well-defined formation energies. As these charged particles travel to the surface of the sample, they lose energy. Using surface-barrier detectors, these energy losses are measured and the  ${}^6\text{Li}$  location, where the nuclear reaction took place, is calculated. For this calculation, the density and composition of the sample through which they pass before emerging from the sample surface has to be considered. For the corresponding experiments, the pristine and coated Li foils (Honjo; battery grade, 50 and 300  $\mu\text{m}$  thickness) were placed within the vacuum chamber of the NDP spectrometer at the CANAM NPI beamline of the LVR15 research reactor in Rez, operating at a reactor power of 10 MW. The NDP spectrum of  ${}^6\text{Li}$  was measured with a single-mode setup utilizing an FDD solid state Canberra detector, Canberra preamplifiers and a Multi-Channel Analyzer. For these measurements, a typical energy resolution was about 2.5 keV per channel. The detector-sample solid angle was set to  $10^{-2}$  rad, which allowed to measure the alpha and triton particles with a counting rate of several tens of particles per second. A 2.8  $\mu\text{m}$  thick Macrofol film was placed between the sample and the detector to separate the alpha and triton signals and increase the resolution of the triton signal. The mass thickness plot was derived from the energy loss plot of the generated alpha and triton particles by assuming a uniform material composition (elemental composition and density) and distribution of Li for the calculation using the SRIM (Stopping and Range of Ions in Matter) software [48]. Fourier-transform infrared (FT-IR) spectroscopy was performed utilizing a Perkin Elmer UATR Two. X-ray photoelectron spectroscopy (XPS) was conducted using a monochromatic Al K $\alpha$  ( $h\nu = 1,487$  eV) X-ray source and a Phoibos 150 XPS spectrometer (SPECS–Surface concept) equipped with a micro-channel plate and Delay Line Detector (DLD). The scans were acquired in a Fixed Analyser Transmission mode with an X-ray power source of 200 W (15 kV), a pass energy of 30 eV and 0.1 eV energy steps. The depth profiling was performed by a focused Ar $^{+}$  gun operating at 5 keV with an ion filter and sputtering rate of 0.8 nm min $^{-1}$ . The CasaXPS software was used for fitting the spectra, using a nonlinear Shirley-type background and 70% Gaussian and 30% Lorentzian profile functions, except for the hydrocarbons (–C–C–/–C–H–) for which an asymmetric peak-shape was employed. All the electrochemical performance tests on the mono-layer cells were conducted with Maccor Series 4000 battery tester. The galvanostatic cycling of the bipolar stacked 2-layer cells was carried out using a multi-channel potentiostat (VMP BioLogic). Electrochemical impedance spectroscopy (EIS) was performed with the same instrument. The frequency range was set to 1 MHz–10 mHz and the AC amplitude was 10 mV. Linear sweep voltammetry was conducted to determine the electrochemical stability of the hybrid electrolyte in PSiO@Li||SS cells. The scan rate was set to 0.5 mV s $^{-1}$  and the temperature was set to 25  $^{\circ}\text{C}$ .

To prepare the samples for the *ex situ* SEM and XPS analysis, the cycled electrodes were recovered by disassembling the cycled Li||NCM $_{88}$  and PSiO@Li||NCM $_{88}$  cells (500 cycles at 1C) in the dry room, washing the electrodes with dimethyl carbonate (DMC) to remove the MILE, and subsequent drying under vacuum to get rid of any residual DMC. In order to avoid any contact with moist air, the *ex situ* samples were transferred via airtight SEM and XPS transfer boxes.

#### Declaration of Competing Interest

The authors declare that they have no known competing financial interests or personal relationships that could have appeared to influence the work reported in this paper.

#### Data availability

Data will be made available on request.

#### Acknowledgement

The authors would like to thank the Federal Ministry for Education and Research (BMBF) for financial support within the FestBatt (03XP0175B), FB2-POLY (03XP0429B), FB2-Hybrid (03XP0428B), LILLINT (03XP0225D), and LISI (03XP0224D and 03XP0224C) project. Financial support from the Helmholtz Association is also kindly acknowledged. Moreover, Z.C., A.I. and S.P. would like to thank the European Commission for financial support within the Marie Skłodowska-Curie grant agreement No 860403 as part of the Horizon 2020 research and innovation programme. NDP measurements were carried out at the CANAM infrastructure of the NPI CAS Rez supported through MEYS project No. LM2015056.

#### References

- [1] H.P. Liang, Z. Chen, X. Dong, T. Zinkevich, S. Indris, S. Passerini, D. Bresser, *Macromol. Rapid Commun.* 43 (2022) 2100820.
- [2] H. Liu, X.B. Cheng, R. Xu, X.Q. Zhang, C. Yan, J.Q. Huang, Q. Zhang, *Adv. Energy Mater.* 9 (2019) 1902254.
- [3] J.B. Goodenough, K.-S. Park, *J. Am. Chem. Soc.* 135 (2013) 1167–1176.
- [4] D. Yan, H.Y. Yang, Y. Bai, *Nano Res.* (2023), <https://doi.org/10.1007/s12274-023-5427-7>.
- [5] R. Xu, Y. Xiao, R. Zhang, X.B. Cheng, C.Z. Zhao, X.Q. Zhang, C. Yan, Q. Zhang, J. Q. Huang, *Adv. Mater.* 31 (2019) 1808392.
- [6] X. Kong, P.E. Rudnicki, S. Choudhury, Z. Bao, J. Qin, *Adv. Funct. Mater.* 30 (2020) 1910138.
- [7] Z. Chen, G.-T. Kim, Z. Wang, D. Bresser, B. Qin, D. Geiger, U. Kaiser, X. Wang, Z. X. Shen, S. Passerini, *Nano Energy* 64 (2019) 103986–103995.
- [8] D. Lin, Y. Liu, Y. Cui, *Nat. Nanotechnol.* 12 (2017) 194–206.
- [9] Z. Chen, X. Gao, J.-K. Kim, G.-T. Kim, S. Passerini, *A.C.S. Appl. Mater. Interfaces* 13 (2021) 53810–53817.
- [10] R. Weber, M. Genovese, A.J. Louli, S. Hames, C. Martin, I.G. Hill, J.R. Dahn, *Nat. Energy* 4 (2019) 683–689.
- [11] M. Balaish, J.C. Gonzalez-Rosillo, K.J. Kim, Y. Zhu, Z.D. Hood, J.L. Rupp, *Nat. Energy* 6 (2021) 227–239.
- [12] F. Laman, K. Brandt, *J. Power Sources* 24 (1988) 195–206.
- [13] A. Varzi, K. Thanner, R. Scipioni, D. Di Lecce, J. Hassoun, S. Dörfler, H. Altheus, S. Kaskel, C. Prehal, S.A. Freunberger, *J. Power Sources* 480 (2020), 228803.
- [14] X. He, D. Bresser, S. Passerini, F. Baakes, U. Krewer, J. Lopez, C.T. Mallia, Y. Shao-Horn, I. Cekic-Laskovic, S. Wiemers-Meyer, *Nat. Rev. Mater.* 6 (2021) 1036–1052.
- [15] M. Keller, A. Varzi, S. Passerini, *J. Power Sources* 392 (2018) 206–225.
- [16] B. Zhang, L. Chen, J. Hu, Y. Liu, Q. Feng, G. Zhu, L.-Z. Fan, *J. Power Sources* 442 (2019), 227230.
- [17] S. Li, S.Q. Zhang, L. Shen, Q. Liu, J.B. Ma, W. Lv, Y.B. He, Q.H. Yang, *Adv. Sci.* 7 (2020) 1903088.
- [18] P. Hartmann, T. Leichtweiss, M.R. Busche, M. Schneider, M. Reich, J. Sann, P. Adelhelm, J. Janek, *J. Phys. Chem. C* 117 (2013) 21064–21074.
- [19] A. Parejiya, R. Amin, M.B. Dixit, R. Essehli, C.J. Jafta, D.L. Wood III, I. Belharouak, *ACS Energy Lett.* 6 (2021) 3669–3675.
- [20] Z. Chen, D. Stepien, F. Wu, M. Zarrabeitia, H.-P. Liang, J.-K. Kim, G.-T. Kim, S. Passerini, *ChemSusChem* 15 (2022) e202200038.
- [21] H.P. Liang, M. Zarrabeitia, Z. Chen, S. Jovanovic, S. Merz, J. Granwehr, S. Passerini, D. Bresser, *Adv. Energy Mater.* 12 (2022) 2200013.
- [22] T. Fujieda, N. Yamamoto, K. Saito, T. Ishibashi, M. Honjo, S. Koike, N. Wakabayashi, S. Higuchi, *J. Power Sources* 52 (1994) 197–200.
- [23] K. Kimura, J. Motomatsu, Y. Tominaga, *J. Phys. Chem. C* 120 (2016) 12385–12391.
- [24] S. Wooh, H.J. Butt, *Angew. Chem.* 129 (2017) 5047–5051.
- [25] J. Meng, F. Chu, J. Hu, C. Li, *Adv. Funct. Mater.* 29 (2019) 1902220.
- [26] O. Wijaya, P. Hartmann, R. Younesi, I.I. Markovits, A. Rinaldi, J. Janek, R. Yazami, *J. Mater. Chem. A* 3 (2015) 19061–19067.

- [27] W. Zhang, Y. Leng, P. Zhao, J. Wang, D. Zhu, J. Huang, *Green Chem.* 13 (2011) 832–834.
- [28] J. Wang, D.X. Liu, M. Canova, R.G. Downing, L.R. Cao, A.C. Co, J. Radioanal. Nucl. Chem. 301 (2014) 277–284.
- [29] E. Moyassari, L. Streck, N. Paul, M. Trunk, R. Neagu, C.-C. Chang, S.-C. Hou, B. Märkisch, R. Gilles, A. Jossen, *J. Electrochem. Soc.* 168 (2021), 020519.
- [30] S. Lv, T. Verhallen, A. Vasileiadis, F. Ooms, Y. Xu, Z. Li, Z. Li, M. Wagemaker, *Nat. Commun.* 9 (2018) 1–12.
- [31] I. Tomandl, J. Vacik, T. Kobayashi, Y. Mora Sierra, V. Hnatowicz, V. Lavreniev, P. Horak, G. Ceccio, A. Cannavo, M. Baba, *Radiat. Eff. Defects Solids* 175 (2020) 394–405.
- [32] Z. Kasztovszky, C. Stieghorst, H.H. Chen-Mayer, R.A. Livingston, R.M. Lindstrom, Prompt-gamma activation analysis and its application to cultural heritage, in: S. D'Amico, V. Venuti (Eds.), *Handbook of Cultural Heritage Analysis*, Springer International Publishing, Cham, 2022, pp. 95–143.
- [33] Z. Chen, D. Steinle, H.-D. Nguyen, J.-K. Kim, A. Mayer, J. Shi, E. Paillard, C. Iojoiu, S. Passerini, D. Bresser, *Nano Energy* 77 (2020), 105129.
- [34] G.T. Kim, G.B. Appetecchi, M. Carewska, M. Joost, A. Balducci, M. Winter, S. Passerini, *J. Power Sources* 195 (2010) 6130–6137.
- [35] Z. Chen, G.T. Kim, J.K. Kim, M. Zarrabetia, M. Kuenzel, H.P. Liang, D. Geiger, U. Kaiser, S. Passerini, *Adv. Energy Mater.* 11 (2021) 2101339–2101354.
- [36] C. Wagner, W. Riggs, L. Davis, J. Moulder, G. Muilenberg, *Physical Electronics Division, Eden Prairie Minn* 55344 (1979).
- [37] G. Beamson, *The Scienta ESCA 300 Database*, (1992).
- [38] K. Smith, K. Black, *J. Vac. Sci. Technol. A* 2 (1984) 744–747.
- [39] A.V.N.C.D. Wagner A. Kraut-Vass J.W. Allison C.J. Powell J.R. Jr N.S. Rumble Reference, Database 20, Version 3.4 2003 <http://srdata.nist.gov/xps/>.
- [40] F. Buchner, M. Bozorgchenani, B. Uhl, H. Farkhondeh, J. Bansmann, R.J.r. Behm., *J. Phys. Chem. C* 119 (2015) 16649–16659.
- [41] H. Kim, F. Wu, J.T. Lee, N. Nitta, H.T. Lin, M. Oschatz, W.I. Cho, S. Kaskel, O. Borodin, G. Yushin, *Adv. Energy Mater.* 5 (2015) 1401792.
- [42] S. Tanuma, C. Powell, D. Penn, *Surf. Interface Anal.* 43 (2011) 689–713.
- [43] E. Markevich, G. Salitra, A. Rosenman, Y. Talyosef, F. Chesneau, D. Aurbach, *J. Mater. Chem. A* 3 (2015) 19873–19883.
- [44] H.W. Kim, P. Manikandan, Y.J. Lim, J.H. Kim, S.-C. Nam, Y. Kim, *J. Mater. Chem. A* 4 (2016) 17025–17032.
- [45] H.W. Kim, J. Han, Y.J. Lim, Y. Choi, E. Lee, Y. Kim, *Adv. Funct. Mater.* 31 (2020) 2002008.
- [46] S.A. Pervez, G. Kim, B.P. Vinayan, M.A. Cambaz, M. Kuenzel, M. Hekmatfar, M. Fichtner, S. Passerini, *Small* 16 (2020) 2000279–2000288.
- [47] S.-H. Kim, K.-H. Choi, S.-J. Cho, J. Yoo, S.-S. Lee, S.-Y. Lee, *Energy Environ. Sci.* 11 (2018) 321–330.
- [48] J.F. Ziegler, M.D. Ziegler, J.P. Biersack, *Nucl. Instrum. Methods Phys. Res., Sect. B* 268 (2010) 1818–1823.